NUCLEAR SCIENCE AND TECHNIQUES **26**, 020102 (2015)

Latest advances of X-ray imaging and biomedical applications beamline at SSRF*

XIE Hong-Lan (谢红兰),[1,†] DENG Biao (邓彪),[1] DU Guo-Hao (杜国浩),[1] FU Ya-Nan (付亚楠),[1] CHEN Rong-Chang (陈荣昌),[1] ZHOU Guang-Zhao (周光照),[1] REN Yu-Qi (任玉琦),[1] WANG Yu-Dan (王玉丹),[1] XUE Yan-Ling (薛艳玲),[1] PENG Guan-Yun (彭冠云),[1] HE You (和友),[1] GUO Han (郭瀚),[1] and XIAO Ti-Qiao (肖体乔)[1,‡]

[1] *Shanghai Synchrotron Radiation Facility (SSRF), Shanghai Institute of Applied Physics, Chinese Academy of Sciences, Shanghai 201204, China*

(Received September 26, 2014; accepted in revised form December 19, 2014; published online April 12, 2015)

On May 6, 2009, the X-ray imaging and biomedical application beamline (BL13W1) at Shanghai Synchrotron Radiation Facility (SSRF) officially opened to users, with 8–72.5 keV X-rays. The experimental station is equipped with four sets of X-ray CCD detectors of different pixel size (0.19–24 μm) for on-line phase-contrast imaging and micro-CT imaging with 0.8 μm spatial resolution and 1 ms temporal resolution. An *in vivo* micro-CT experiment for a living insect was realized in 4 s. An X-ray fluorescence detector is equipped for X-ray fluorescence mapping imaging and X-ray fluorescence micro-CT imaging with 50 μm spatial resolution. In order to meet different requirements from the users, several experimental methods, such as X-ray spiral micro-CT, X-ray local micro-CT, X-ray fast micro-CT, X-ray grating-based differential micro-CT, X-ray fluorescence micro-CT and X-ray quantitative micro-CT have been developed, and nearly 60 papers related to those developments for this beamline have been published. Moreover, the beamline has realized the remote fast CT reconstruction, providing a great convenience for the users to process experimental data at their offices. As of August 2014, the beamline has offered the user beamtime of (23 145 h), from which 232 user papers have been published, including 151 SCI papers and 55 papers with SCI impact factor > 3. The quantity and quality of the user paper outcome keep a steady increase. Some typical user experimental results are introduced.

Keywords: X-ray imaging, X-ray in-line phase-contrast imaging, X-ray micro-CT, CT reconstruction, X-ray fluorescence CT

DOI: 10.13538/j.1001-8042/nst.26.020102

I. INTRODUCTION

The beamline of X-ray imaging and biomedical applications (BL13W1) at Shanghai Synchrotron Radiation Facility (SSRF) devotes itself to dynamic in-line X-ray phase-contrast imaging (IL-PCI), X-ray microscopic computerized-tomography (Micro-CT) and other new techniques of X-ray imaging, such as X-ray fluorescence computed tomography (XFCT), grating-based differential phase-contrast imaging (GDPC), fast micro-CT, local micro-CT and spiral micro-CT. The beamline has two categories of applications, (1) low dose, non-destructive, high resolution, dynamic or 3-dimensional (3D) X-ray phase-contrast imaging for the inner microstructure of soft tissues and low Z materials [1–3]; and (2) non-destructive, high resolution, 3D X-ray absorption imaging for the inner microstructure of palaeontology, archaeology and geology samples. Its construction began on Dec. 25, 2004 and was completed in April of 2009, achieving all the design goals, as shown in Table 1. Since then, it has become a powerful experimental platform for interdisciplinary studies in biomedicine, materials science, archaeology and other fields in China.

As of August 2014, the beamline kept a high efficiency and a low-fault operation (Table 2), running a total beamtime of (28 246 h) with a low average fault rate of 1.3%. About 82% (23 145 h) of the beamtime were provided to about 3200 users from 782 proposals in biomedicine, materials science, archaeology, environmental and earth sciences, physics, industry applications and so on. The approval rate of beamtime applications was 25%, and 232 papers were published by the users. The other (5101 h) of beamtime were used for in-house research and methodology developments, from which 51 papers were published.

II. BEAMLINE

A sketch layout of the beamline is shown in Fig. 1. The light source is a hybrid-type wiggler of eight periods in periodic length of 14 cm. The maximum K-value is 24.8 at minimum gap (17 mm) of the wiggler magnet. Energy range of the synchrotron radiation is 8–72.5 keV, corresponding to the gaps from 17 mm to 35 mm. A white beam slit is placed at 20 m away from the source point. The maximum aperture is 30 mm × 4 mm. The high heatload of 10 kW is a big challenge for the beamline.

In order to reduce heatload on the downstream Be window and double crystal monochromator, a 6-axis highly-oriented pyrolytic graphite (HOPG) filter was developed (Fig. 2). It consists of six water-cooled filter banks, each having two beam apertures blocked with two HOPG foils and being mounted to an individual actuator. HOPG was chosen as the filter material because it has a high thermal conductivity and a smooth natural surface to keep a good coherence of the beam for phase-contrast imaging. Several filter foils of different thickness can be combined into the beam for different wiggler gaps, beam currents and energy ranges, to keep

* Supported by the National Natural Science Foundation of China (Nos. 11475248 and 11105213)

† Corresponding author, xiehonglan@sinap.ac.cn

‡ Corresponding author, tqxiao@sinap.ac.cn

TABLE 1. Acceptance test results of designed goals

Specifications			Design goals	Test results
Energy range (keV)			10–60	8–72.5 keV
Energy resolution ($\Delta E/E$)			$< 5 \times 10^{-3}$	$< 3 \times 10^{-3}$
Maximal beam size (mm@32 m@20 keV)			45 (H)×5 (V)	48 (H)×5.3 (V)
Photon flux density (phs/s mm^2) @20 keV@200 mA			1×10^9	1.9×10^{10}
Spatial resolution (μm)	Phase-contrast imaging	Dynamic	≤ 20 @5 frame/s	15 @6.5 frame/s
		Static	≤ 5	3.0
	Absorption contrast imaging		≤ 3	1.5
	Phase-contrast CT imaging		≤ 20	9.5
	Absorption-contrast CT imaging		≤ 10	9.5

TABLE 2. Summary of BL13W1 operation (2009.05.06-2014.08.31)

Items	2009	2010	2011	2012	2013	2014(Jan.-Aug.)	Total
Provide beamtime (h)	3388	5248	5384	5370	5400	3456	28246
User beamtime (h)	2500	4408	4375	4641	4497	2724	23145
In-house beamtime (h)	888	840	1010	728	903	732	5101
Approved user proposals	94	141	148	149	151	99	782
User publications	4	24	35	51	56	60	232
Fault rate (%)	2.60	1.69	2.47	0.10	0.70	0.10	1.30

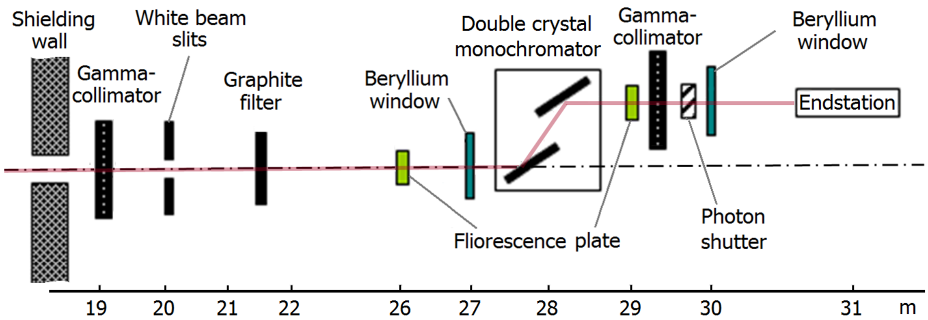

Fig. 1. (Color online) Sketch layout of Beamline BL13W1.

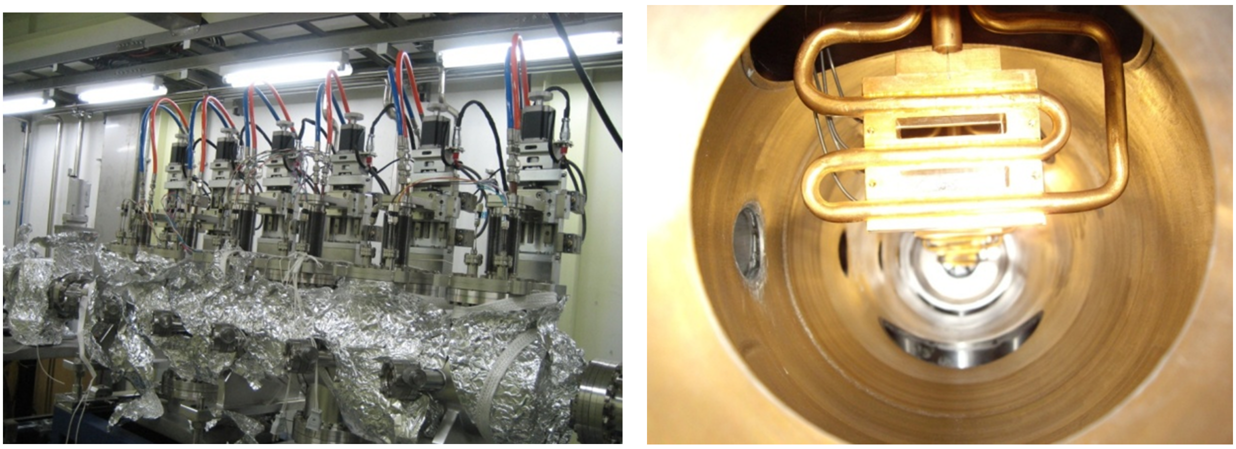

Fig. 2. (Color online) The whole structure (a) and inside structure (b) of the filter.

a high flux output on samples in the entire photon energy range. The constant-exit double crystal cryogenically-cooled monochromator is placed at 28 m from the source point. In the monochromator, two sets of Si (111) and Si (311) crystals can be exchanged on-line.

TABLE 3. Parameters of X-ray CCD detectors on the BL13W1 endstation

X-ray CCD detectors		Objective lens	Pixel size /μm	Field of view /mm	Scintillator (thickness /μm)
Optique Peter, PCO2000		1x	7.4	15 × 5	Yag:Ce (100)
		1.25x	5.92	12 × 5	Yag:Ce (100)
		2x	3.7	7.6 × 5	Yag:Ce (100)
		4x	1.85	3.8 × 3.8	Yag:Ce (50)
		10x	0.74	1.5 × 1.5	Yag:Ce (50)
		20x	0.37	0.8 × 0.8	Yag:Ce (20)
		40x	0.19	0.4 × 0.4	Yag:Ce (20)
Hamamatsu Flash4.0	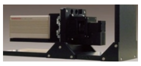	AA50	0.65	1.33 × 1.33	GdOS:Tb (10)
			2.25	2.3 × 2.3	GdOS:Tb (10)
		AA40	6.5	13 × 5	LSO:Ce (10)
Photonic Science, VHR			9	36 × 5	GdOS:Tb
			13	45 × 5	GdOS:Tb
Princeton Instruments, Quad-RO 4320			24	45 × 5	GdOS:Tb

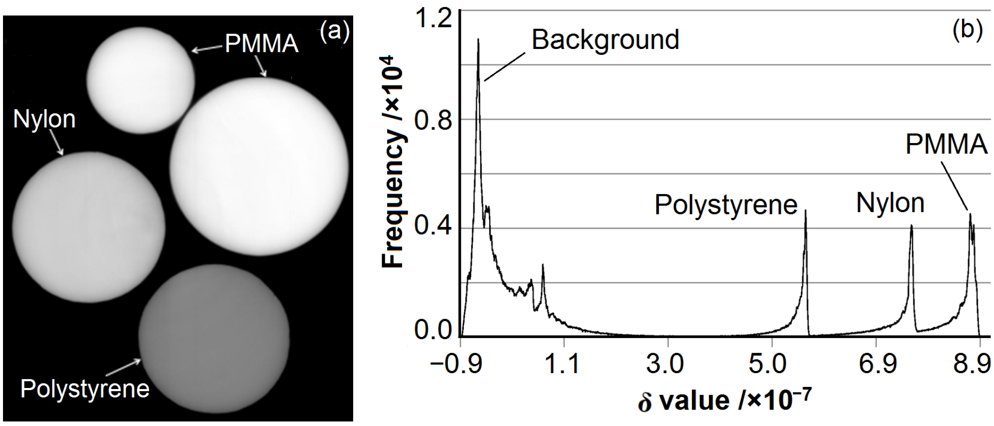

Fig. 3. Reconstructed result of the wire sample (a) and its histogram (b).

III. ENDSTATION

The endstation consists of two flexible experimental tables of 2.5 m and 5.0 m in length. The rail on the tables is used to adjust the sample–detector (CCD) distance. The sample stage allows translation in three dimensions with a resolution of better than 1 μm, and rotation in three axes with the max speed of $\theta_z = 90°/\text{s}$. Ionization chambers are used to monitor intensity of incident X-ray.

Four kinds of X-ray CCD detectors of different spatial resolutions from 0.19 μm/pixel to 24 μm/pixel for different samples can be used. Field of view (FOV) of the X-ray CCD detectors can be up to 45 mm (H) × 5 mm (V) at the maximal beam size on the sample. Table 3 shows the pixel size and field of view of X-ray CCD detectors on the BL13W1 endstation. Dynamic imaging experiments with spatial-temporal resolution of 9 μm/pixel @ 20 frame/s. Micro-CT experiments with spatial resolution of 0.37 μm/pixel have been realized. An X-ray fluorescence detector with the spatial resolution of 50 μm is used for developing X-ray fluorescence micro-CT (XFCT) method and X-ray fluorescence mapping method. The users can perform dynamic absorption or phase-contrast imaging, absorption or phase-contrast micro-CT, XFCT etc. on the endstation.

IV. METHODOLGY DEVELOPMENT

According to the users' demands, 13 X-ray imaging methods were developed, as shown in Table 4.

We have realized local and remote fast micro-CT reconstruction. The fast micro-CT reconstruction for a set of 1000 projections takes only 5 min. The remote fast micro-CT reconstruction system has been opened to users, bringing much convenience for users to treat experimental data at their offices. X-ray quantitative phase-contrast micro-CT has been realized and some achievements of phase retrieval methods of IL-PCI have been published [4–6]. XFCT, GDPC, spiral micro-CT and local micro-CT method have been built. X-ray multi-energy micro-CT combined with data-constrained modeling (DCM) for quantitative analysis of materials has been developed. Other X-ray imaging methods, such as low dose and fast micro-CT imaging based on equally sloped tomography (EST) and coherent X-ray diffraction imaging

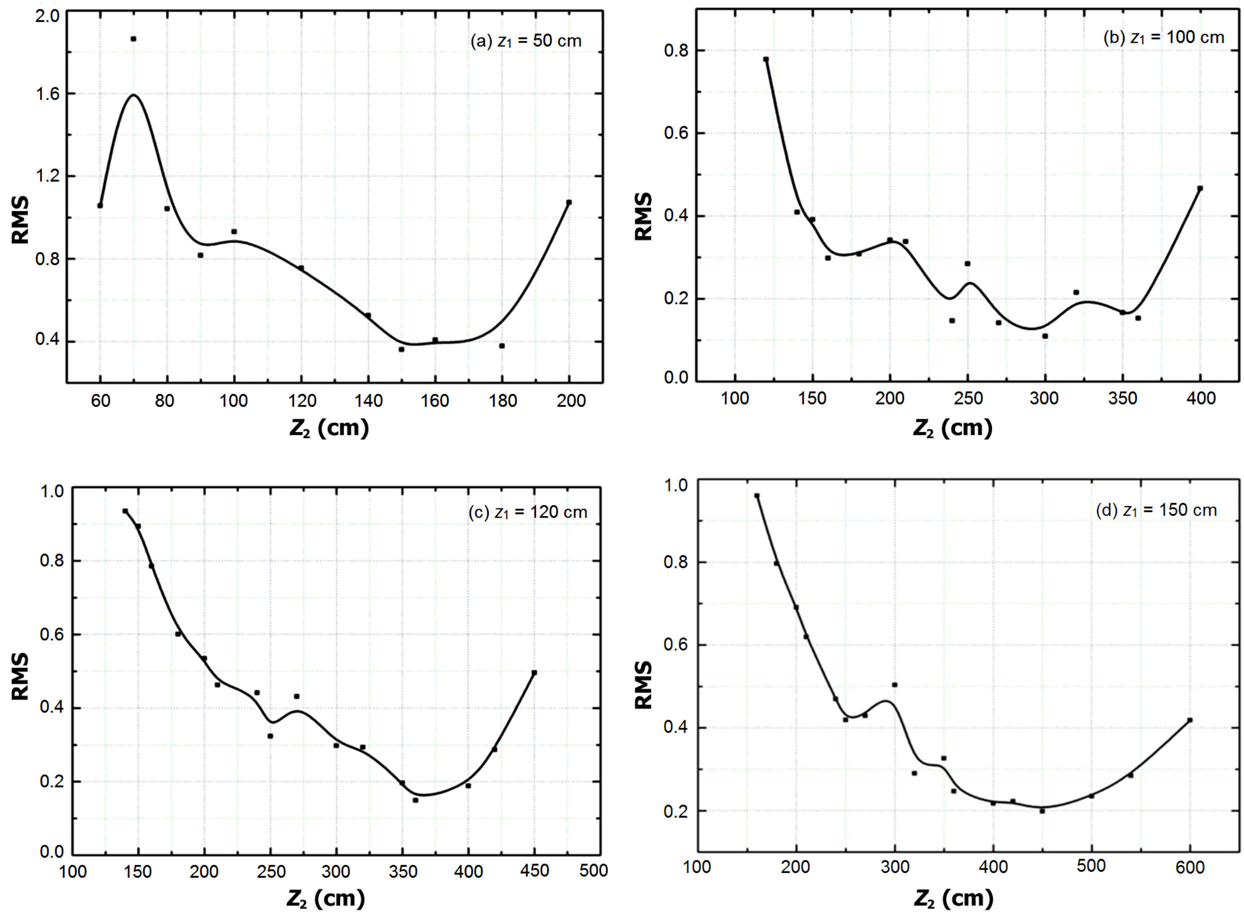

Fig. 4. Retrieving error vs. Z_2, with Z_1 being set to (a) 50 cm, (b) 100 cm, (c) 120 cm and (d) 150 cm.

TABLE 4. Summary of techniques and methods developed for user experiments on the BL13W1 beamline

Requirements from user experiments	Techniques and methods developed for user experiments
To speed up experimental data processing and to make it more convenient to users	A fast CT reconstruction system; A remote fast CT reconstruction system; A lab for image processing
To improve image quality and to obtain quantitative 3D structural information of samples	Phase retrieval methods for IL-PCI; Grating-based differential phase-contrast imaging(GDPC); Multi-energy micro-CT combined with data constraint model; Ring artifacts correction for CT reconstruction
To reduce CT data-collection time and dose on samples	Fast micro-CT based on equal sloped tomography (EST) reconstruction algorithm; Fast micro-CT based on compressed sensing (CS) reconstruction algorithm
To image elemental distributions of samples	X-ray fluorescence CT (XFCT), X-ray fluorescence mapping
3D structural distributions of long samples	Spiral micro-CT
3D structural distributions of large samples	Local micro-CT

(CDI), are being developed. Moreover, the BL13W1 provides users with the ring artifacts correction software for micro-CT reconstruction.

A. Quantitative phase-contrast micro-CT

Three methods have been developed for quantitative in-line phase-contrast micro-CT: (1) phase retrieval with a single distance propagation-based phase-contrast computed tomography (PPCT) data, (2) phase retrieval with two distances PPCT data, and (3) phase retrieval based on phase-attenuation duality (PAD), respectively [4–6]. Performance of different single sample-to-detector distance (SDD) phase retrieval algorithms was studied [7].

An approach was developed to determine the absorption correction factor (ACF) accurately for the Modified Bronnikov algorithm (MBA) to direct reconstruct 3D-refractive

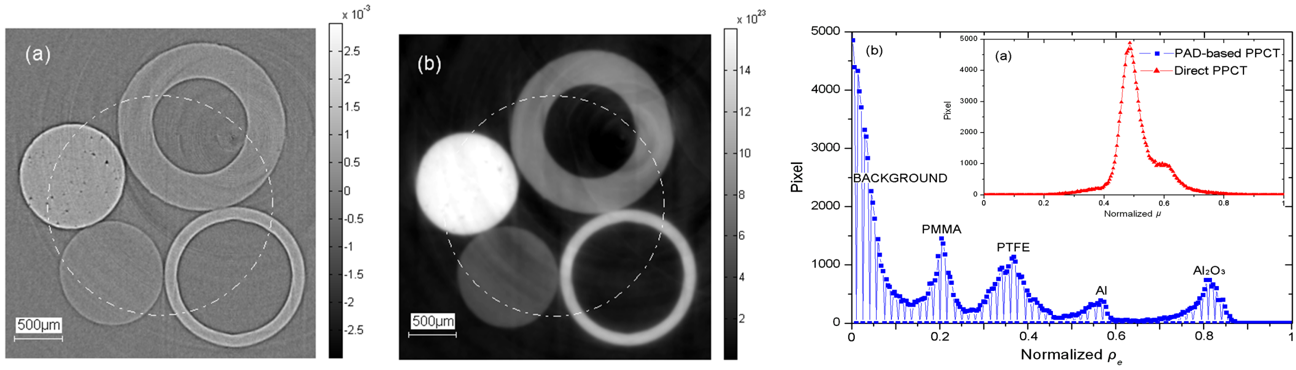

Fig. 5. (Color online) Reconstructions and histograms of electron density distribution of samples by direct (a) and PAD-based (b) PPCT at 60 keV.

index from single SDD X-ray PPCT data [1]. It takes into account the wavelength, SDD and phase-attenuation duality of PPCT. The method was evaluated with a sample of nylon, polystyrene and PMMA fibers. Fig. 3(a) shows the reconstructed result, Fig. 3(b) shows histogram of Fig. 3(a), and the results indicate that three materials are well distinguished.

Compared with phase retrieval with a single distance, phase retrieval with two SDD images can improve the precision apparently in quantitative X-ray in-line phase contrast imaging. However, a critical point that determines the retrieval efficiency of this method is optimization of SDD z_1 and z_2. We investigated the problem systematically based on computer simulation and related experiments. The results show that the highest retrieving precision could be obtained while $z_2 = 3z_1$, as shown in Fig. 4 [5].

Extending validity of the phase-attenuation duality (PAD) method, the PPCT at 60 keV of synchrotron radiation for a sample with both light and dense components was investigated. The results show that the PAD-based PPCT is effective in imaging simultaneously the weak and strong absorption components. Compared with the direct PPCT technique, the PAD-based PPCT technique demonstrates its excellent capability in material discrimination and characterization (Fig. 5) [6].

B. Spiral micro-CT

The maximum beam size of BL13W1 is 45 mm × 5 mm. For a long sample, it is difficult to obtain 3D images in one single CT scan. SR-based spiral micro-CT (SRS micro-CT) is able to obtain volumetric projection data of a long sample in one continuous scan, which is advantageous in its short acquisition time, high spatial resolution and less moving artifacts. An SRS micro-CT system has been built on BL13W1 [8]. SRS micro-CT of bamboo was performed. The 3D image and slices were of high spatial resolution, as shown in Fig. 6. The length of scanned bamboo was 10.54 mm, which is 2.73 times of vertical beam size. The inner fiber structures can be seen clearly.

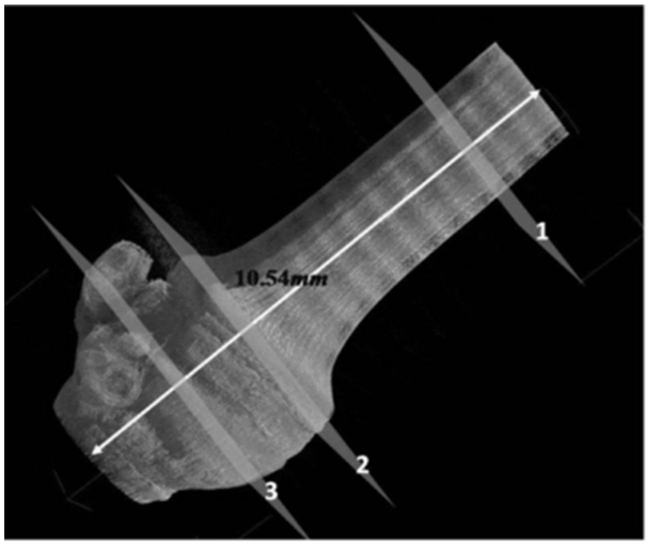

Fig. 6. (Color online) SRS micro-CT reconstructed images of bamboo.

C. X-ray Fluorescence CT

X-ray fluorescence computed tomography (XFCT) allows non-destructive reconstruction of elemental distribution in a sample. The XFCT system was established and experiment results were obtained [9, 10].

In this system, horizontal scanning geometry is used, with an energy-sensitive detector coupled to a multichannel analyzer to register the fluorescence signals simultaneously. A water-cooled X-ray CCD camera is used for direct imaging and alignment purposes. The XFCT system has been opened to public service. XFCT was applied to the reconstruction of a naturally dried cirrhotic liver of the Sprague-Dawley (SD) rat to investigate the distributions of Fe and Zn [11] (Fig. 7). Recently, ordered-subsets expectation maximization (OSEM) algorithm has been introduced into XFCT to speed up the data acquisition process. We are now studying accelerating X-ray fluorescence CT based fast scanning and OSEM (Fig. 8).

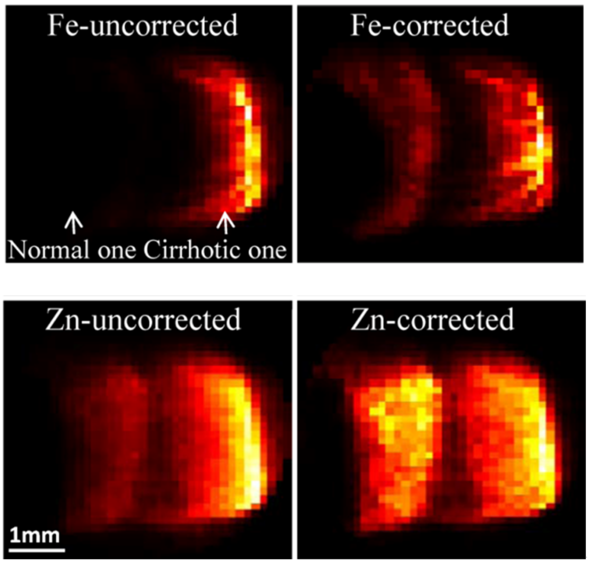

Fig. 7. (Color online) Fe and Zn distributions in the liver of an SD rat.

D. Local micro-CT

An improved algorithm, pseudo-global tomography, is proposed to solve the local CT reconstructing problem. In order to compensate the lost part of projections in the local CT, an effective strategy is applied to reduce DC-shift and low-frequency artifacts caused by projection truncation. With the new algorithm, one is able to reconstruct the correct inner structure of the sample among all the region of interest (ROI) areas regardless of the location of the ROI in the sample without prior knowledge of it, as shown in Fig. 9 [12].

E. Grating-based differential phase-contrast imaging

For low-Z materials, X-ray grating-based differential phase contrast imaging is of higher sensitivity than conventional X-ray imaging [13]. A set of X-ray grating-based imaging system, with one phase grating and one transmission grating, was installed on this beamline. Using the double-grating system, the complex coherence factor was measured and the transverse coherence length and source size were analyzed [14]. The reconstructed slices of absorption coefficient, decrement of the real part of refractive index and scattering coefficient of a mouse brain were obtained (Fig. 10) [15]. Without any staining, various tissues, such as caudate putamen (CPu), lateral ventricle (LV) and corpus callosum (cc), were distinguished in the reconstructed slices.

F. Fast micro-CT based on EST

In order to reduce the absorbed dose and speed up the data collection time for micro-CT, we developed a low dose and fast imaging system based on equally sloped tomography (EST). In traditional filtered back projection (FBP)-based micro-CT, a large number of projections are needed to ensure high spatial resolution, which results in long exposure time and high absorbed dose.

EST-based micro-CT can be applied to solve these problems. In method, the projections are equally sloped angled, not equally spatial angled. The reconstruction results of a cement material by FBP from 1000 projections and EST from 250 projections are shown in Fig. 11. It can be seen that a comparable image quality is achieved by EST with only 1/4 of the projections by FBP. Based on EST, *In vivo* micro-CT with 75% dose reduction and high pressure micro-CT with incomplete angle range of projections (samples in the diamond-anvil cell) have been realized on BL13W1. An *In vivo* micro-CT experiment for a living insect was realized in 4 s. The radiation dose on the sample was 1.69 Gy and the dose absorbed by the insect was 0.67 Gy. If we used equal angle tomographic method such as the FBP algorithm, at least 720 projections would be needed for this case, and the radiation dose would be 3.6 times higher. The EST-based micro-CT imaging system will open to users soon.

G. Multi-energy micro-CT combined with DCM

A data-constrained modelling (DCM) method with multi-energy CT data sets was developed for characterizing sub-resolution compositional microstructures, enabling one to obtain quantitative compositional fractions on each image voxel. The approach has been successfully applied to characterize and predict the microstructure of a range of different materials, including distributions of zinc corrosion product and mineral phases in hydrocarbon reservoir limestone [16, 17]. Microscopic 3D chemical distributions of a corroded zinc wire are shown in Fig. 12. This result is important for understanding the cathodic and anodic processes that occur during corrosion, and is vital when attempting to control the overall rate of corrosion. Also, 3D distributions of dolomite and calcite in a limestone sample were obtained.

H. Local and remote fast micro-CT reconstruction

Fast CT reconstruction system was established at BL13W1. The CT reconstruction can be completed in 5 min, and remote data processing and transfer is realized. The system includes two parts: GPU parallel computing server and CT reconstruction software. The configuration of N-vidia Tesla C2050 with 448 GPU cores is 112 times faster than a 4-core CPU. The fast CT reconstruction software X-TRACT SSRF was developed by international cooperation of SSRF with CSIRO of Australia. Now it opens to users with about 100 registered users. These users can visit the website `https://ct.ssrf.ac.cn`, and download the client software X-TRACT SSRF.

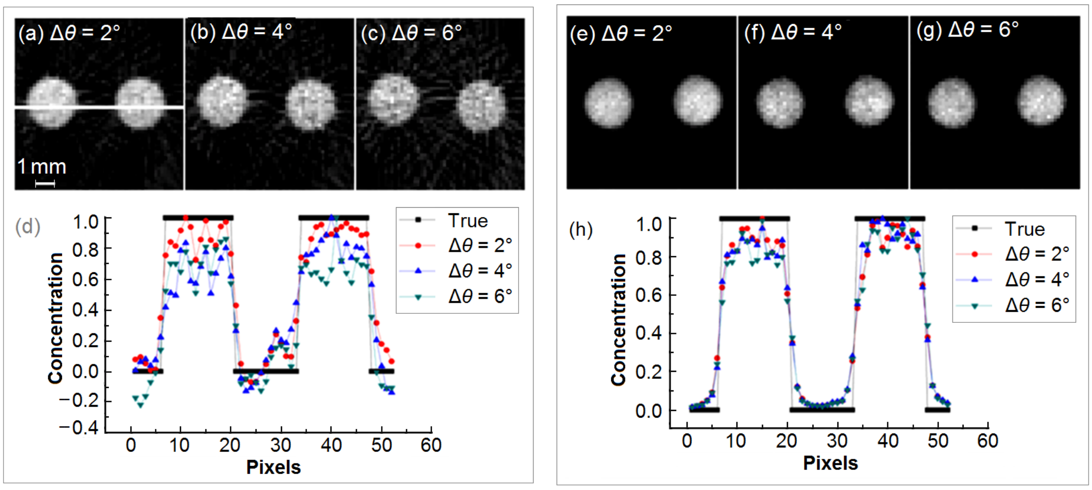

Fig. 8. (Color online) Cd distribution in test sample with different algorithm Left, filtered back projection; right, OSEM.

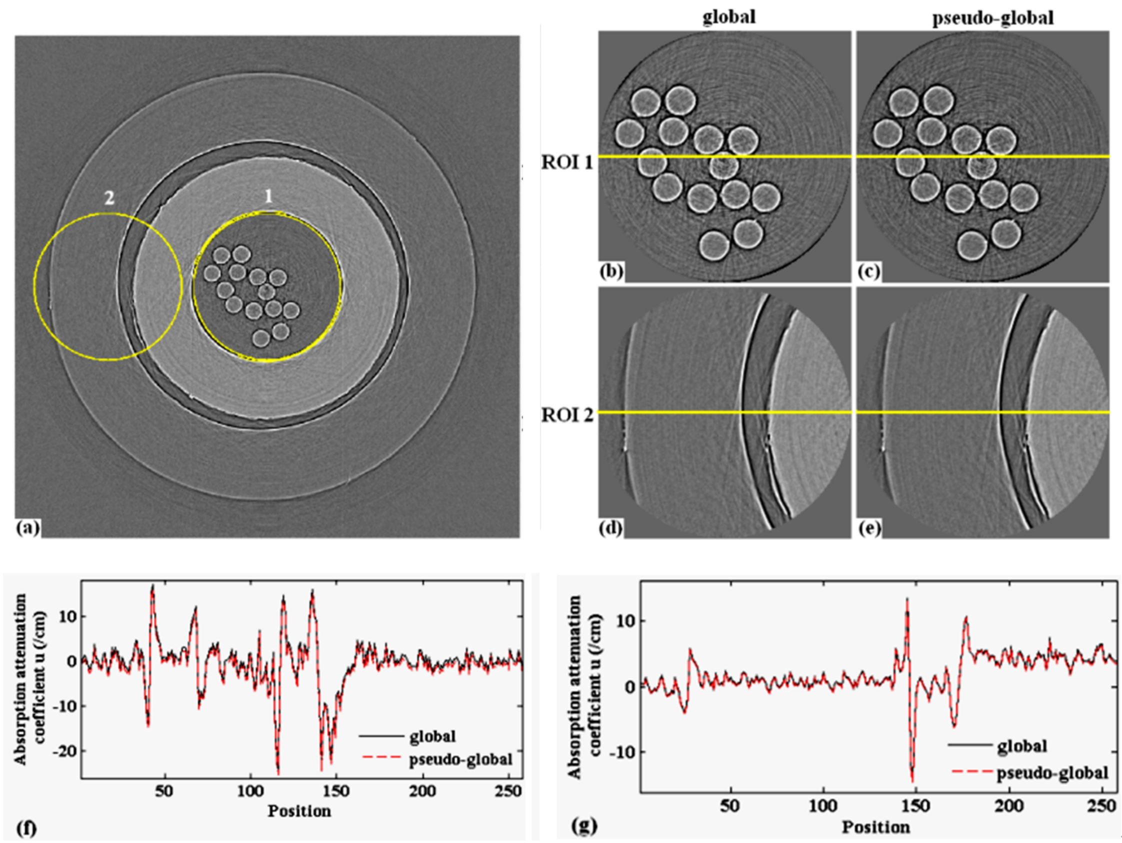

Fig. 9. (Color online) Experimental results of a phantom. (a) the global CT slice for the whole sample; (b) & (d), the ROIs taken from the global reconstruction with 258×258 pixels; (c) & (e), ROIs reconstructed by Pseudo-global tomography; (f) & (g) the profiles (yellow lines).

I. Ring artifacts correction for CT reconstruction

Caused by non-uniform response of detector elements and instabilities of light source, ring artifacts in CT slices greatly influence three-dimensional reconstruction and quantitative analysis. A correction algorithm based on polar-coordinate transform and Fourier transform is proposed for elimination of the ring artifacts [18]. Experimental results indicate that this algorithm not only eliminates the ring artifacts effectively, but also keeps the image edges and increases the signal-to-noise ratio (Fig. 13). The ring artifacts correction software for

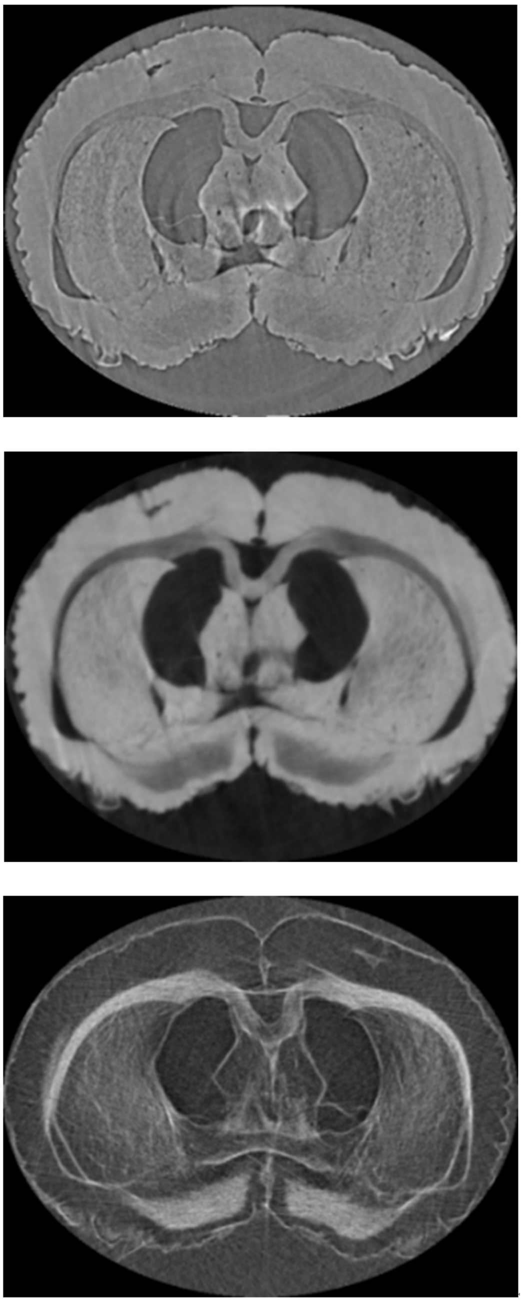

Fig. 10. Reconstructed slices of absorption coefficient, real part decrement of refractive index and scattering coefficient of a mouse brain.

micro-CT reconstruction is based on the correction algorithm, it has been developed and opened to the users.

V. APPLICATIONS

Experimental results of typical applications of BL13W1 will be introduced in this section.

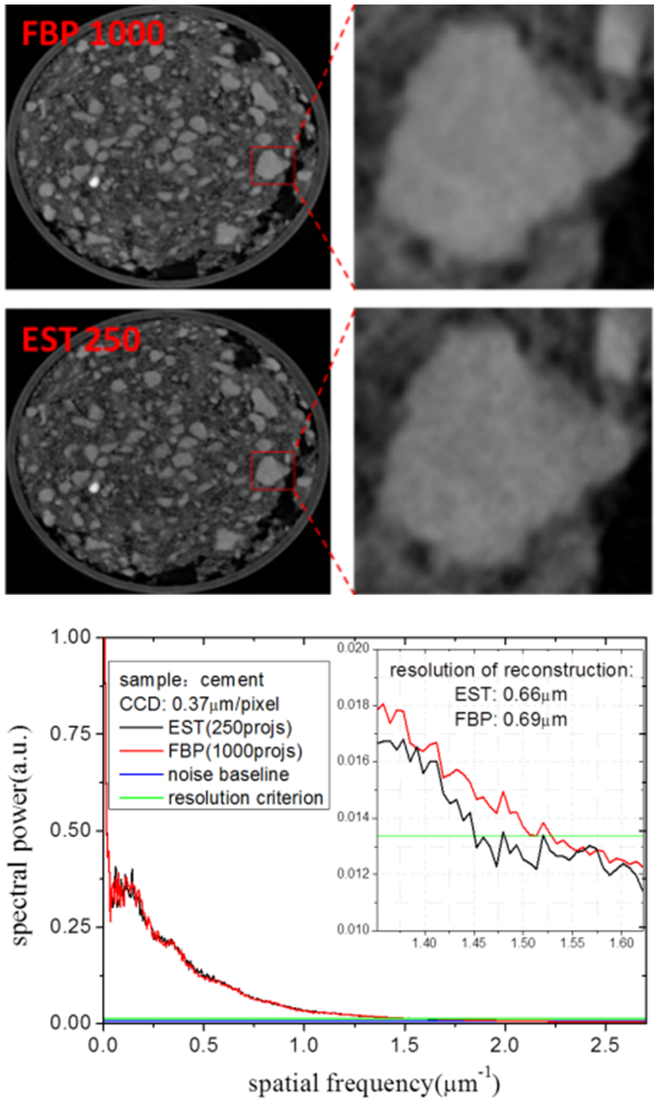

Fig. 11. (Color online) A comparison between the reconstruction results of FBP and EST.

A. Biomedicine

BL13W1, of large beam size, high energy level and high coherence, achieves high resolution imaging for inner microstructure of soft tissues and low Z materials, and dynamic imaging for living animals in biomedicine. Users have carried out researches in different areas, including tumour diagnosis and treatment, nervous system, imaging methodology of phase contrast, safety of synchrotron radiation-based medical imaging, biomedical materials, scar of dermal tissue, acupuncture points, pharmaceutics etc [19–27].

Synchrotron radiation angiography provides a novel solution to directly monitor the success of middle cerebral artery occlusion. Twenty adult SD rats for middle cerebral artery occlusion models with different suture head silicone coating were prepared randomly, and the *In vivo* imaging experiment was performed on BL13W1 [28]. Silicone-coated suture is

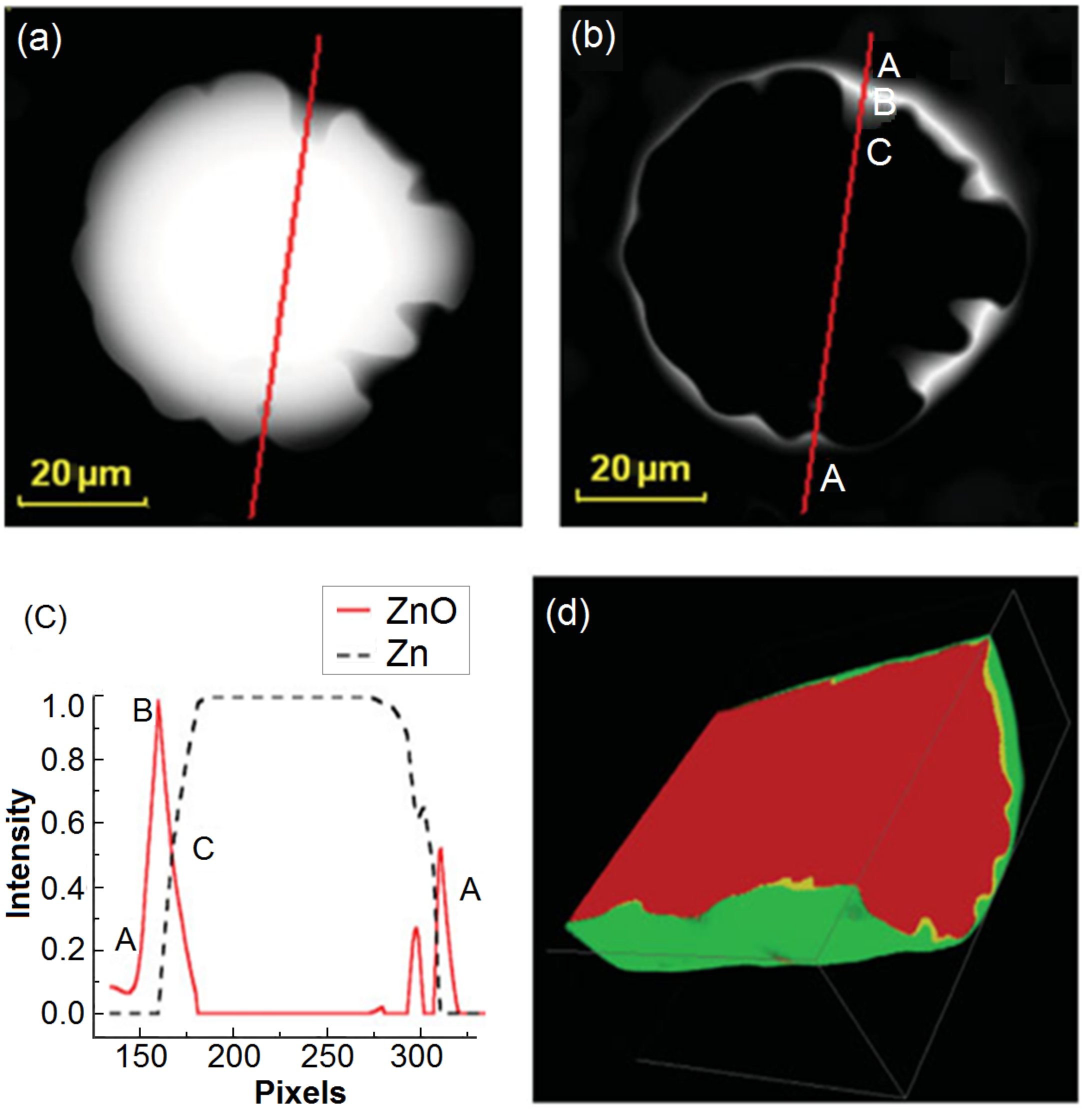

Fig. 12. (Color online) DCM-predicted microstructures: a cross section of a corroded zinc wire. (a) Zn, (b) ZnO, (c) the compositional volume fractions. (d) 3D compositional image.

superior to uncoated suture for producing consistent brain infarction. Additionally, silicone coating length is an important variable controlling the extent of ischemic lesion: infarcts affected predominantly the caudate-putamen with large variability ($<$ 2 mm), both the cortex and caudate-putamen (2–3.3 mm), and most of the hemisphere, including the hypothalamus ($>$ 3.3 mm), as shown in Fig. 14.

TIEG1 (TGFβ inducible early gene 1) can induce apoptosis of cancer cells, but its role in inhibiting invasion and metastasis has not been reported and is unclear. The decreased TIEG1 expression is associated with increased EGFR (epidermal growth factor receptor) expression in breast cancer tissues and cell lines [29]. TIEG1 significantly inhibits breast cancer cell invasion, suppresses mammary tumorigenesis in xenografts in mice, and decreases lung metastasis by inhibition of EGFR gene transcription and the EGFR signaling pathway. The microangiography experiment for blood vessels was performed at BL13W1. The results show that TIEG1 binds the EGFR promoter to inhibitor its transcription, hence the reduction of VEGF and the neovascularization (Fig. 15).

The regenerative treatment of large osseous defects remains a formidable challenge in orthopedic surgery today. Particularly, strategies to control the appropriate degradation rate adapting to the tissue reconstruction are essential for tissue regeneration. The osteoinductive growth factor, recombinant human bone morphogenetic protein-2 (rhBMP-2) was incorporated into calcium/magnesium-doped silica-based scaffolds [30], disulfide-containing PEG-based scaffolds [31], calcium silicate/calcium phosphate cement scaffolds [32], gelatin sponges based implant loaded with nanoparticle [33] for bioactivity and biodegradation promotion. The *in vivo* effects of scaffolds in rabbit radius or fe-

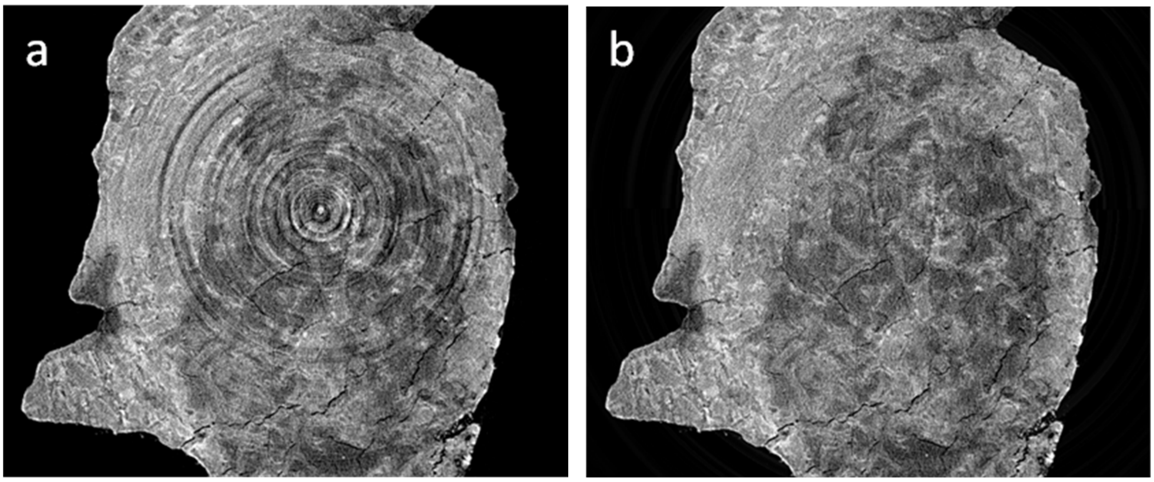

Fig. 13. Fossil slices before (a) and after (b) ring artifacts correction.

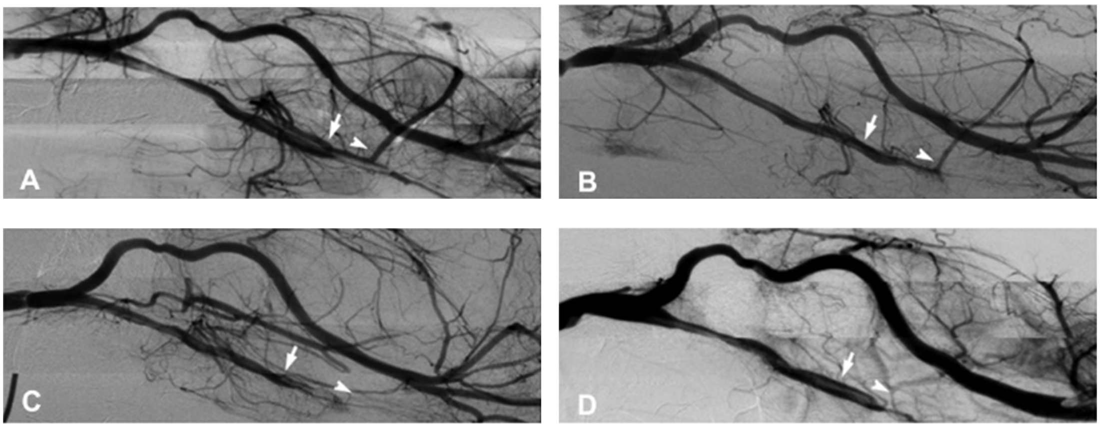

Fig. 14. Synchrotron radiation angiography images of middle cerebral artery (MCA) occlusion using silicone coated sutures with different coating lengths. The MCA was only partially occluded when the suture head was not coated (A) or the coating length was $<$ 2 mm (B). The MCA was successfully occluded when the coating length was 2.0 mm to 3.3 mm without affecting the hypothalamic artery (HTA), posterior cerebral artery (PCA), and anterior choroidal artery (AChA; C). The MCA was occluded when the coating length $>$ 2 mm together with AChA/PCA, and HTA (D).

mur critical defect model were investigated by synchrotron radiation-based micro-computed tomography (SR micro-CT) imaging. The results indicate that the scaffolds underwent gradual resorption and replacement by new bone and induced reunion of bone marrow cavity in 12 weeks, much better than the effect of self-repairing group (Fig. 16). Both osteoinduction and appropriate degradation played a crucial role in accelerating and promoting bone augmentation and effective proangiogenesis.

B. Archaeology and Paleontology

In archaeology, to protect important culture heritage, noninvasive characterization of 3D CT can acquire high-resolution inner structure of a sample. Eye bead, an article of western Asia style, is an evidence of East-West culture communication during the Warring State Period (475BC-221BC), but its production technology needs exploration. SR-μCT was used for the first time to obtain 3D images of an eye bead samples (Fig. 17). The ablate air bubble was found that will not appear in the normal glass phase, and the inlay production technology of eye bead was testified according to micro analysis [34]. By using scanning electron microscope and SR-μCT, crustacean fossils mainly focusing on a few phosphatocopines with nearly complete preservation of stalked eyes, antennula and limbs were examined successfully [35].

C. Materials science

BL13W1 provides hard X-rays of 8–72.5 keV to reveal inner microstructure of the samples nondestructively. And its high flux ensures observation of dynamic process of materi-

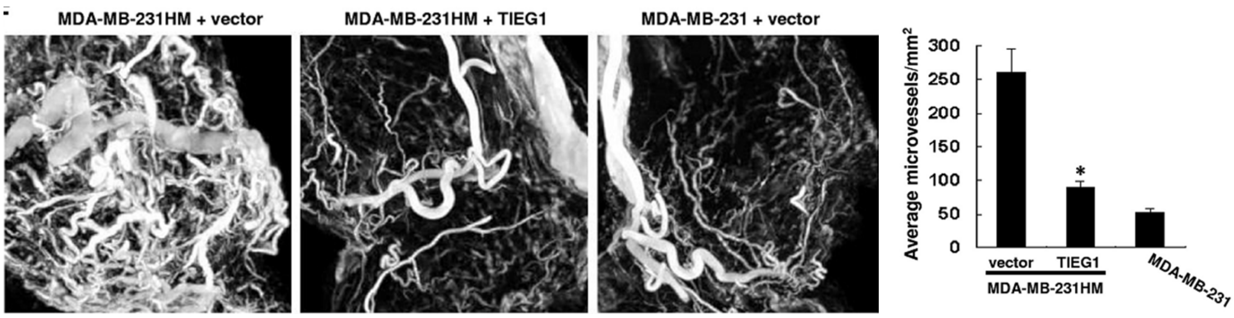

Fig. 15. Synchrotron radiation angiography images of blood vessels and quantification of microvessel density of tumor sections in the mice bearing MDA-MB-231HM/TIEG1, MDA-MB-231HM/Vector, and MDA-MB-231 cells.

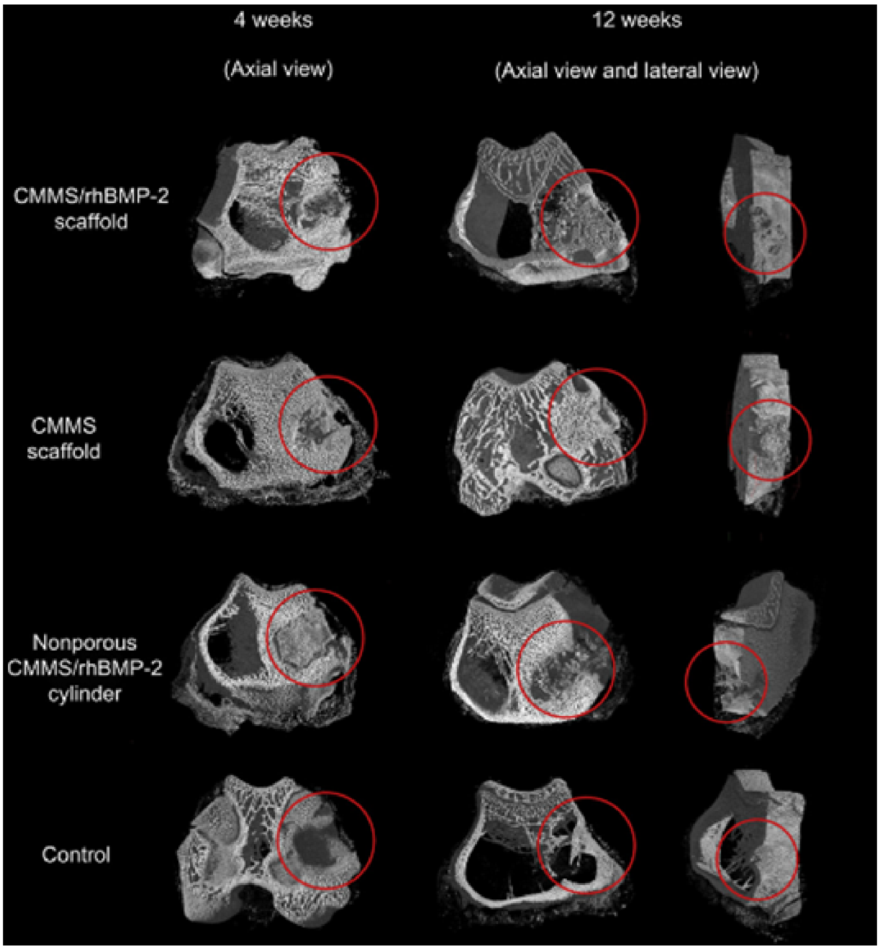

Fig. 16. 3D reconstruction of cross-section images by SR-µCT at week 4 and 12 after scaffolds implant in the rabbit femur.

als structure. Users performed studies on dendrite growth behaviour in the solidification process of metallic alloy [36, 37], hydrogen evolution in the electrochemistry reaction [38], intermetallic compound (IMC) growth behaviour and evolution rule of the bubbles in soldering process at the brazing interface [39, 40], etc. SR micro-CT can be used for characterizing the 3D structure of materials, such as 3D dendrite structure of alloy [41], composites and their distribution of cement in the different hydratation stages, the influence of foaming technology on the porous structure of polymer [42], the change of volume and density for materials in extreme condition of high pressure. Fast micro-CT based on EST or CS reconstruction algorithms can realize the evolution researches of 3D structures for materials.

Combining synchrotron-based computed tomography with scanning electron microscopy-ultramicrotomy, the distribution of micrometer-sized inorganic particles within a polymer matrix was studied [43]. It was found that the inorganic parti-

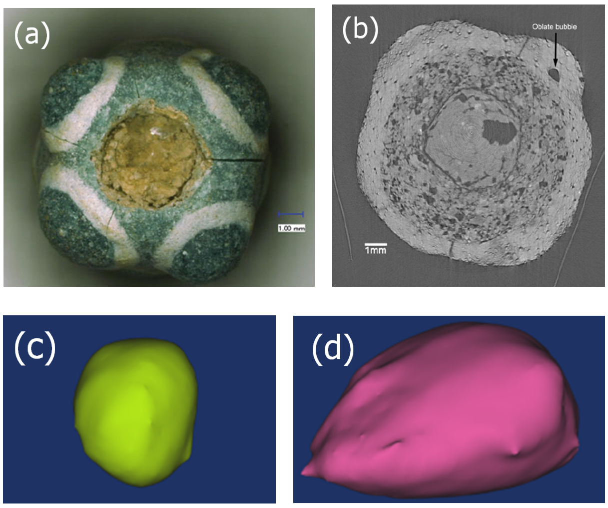

Fig. 17. (Color online) (a) View of sample from the perforation, (b) one transverse section with outlined white layers, (c) 3D reconstruction of a spherical air bubble in the glass phase, (d) 3D reconstruction of an oblate air bubble located at the boundary of a horned eye and glaze.

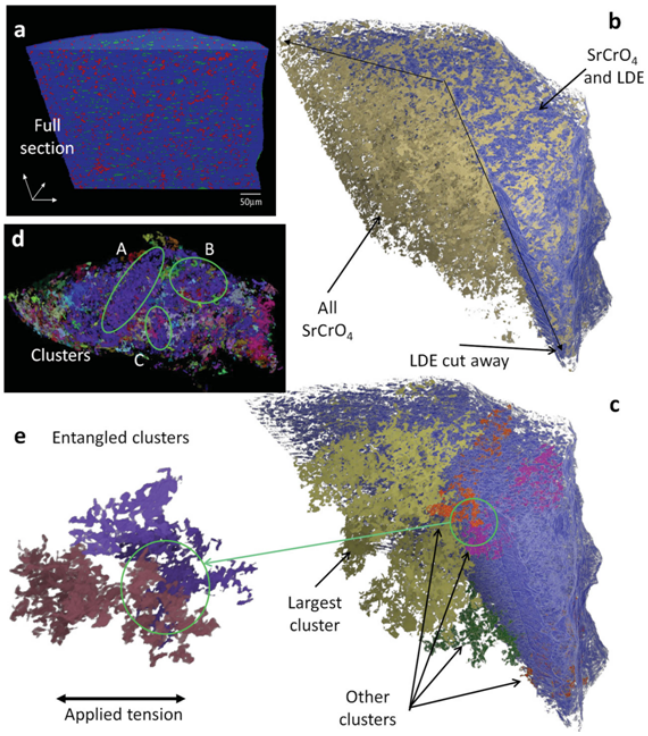

Fig. 18. (Color online) Embedded Fractal Clusters: (a) section through composite containing $SrCrO_4$ (red) embedded in an epoxy matrix with two densities nominated as low density or LDE (green) and normal (blue); (b) 3D reconstruction of LDE (partially cut away) and all the $SrCrO_4$ particles; (c) 3D reconstruction of LDE (partially cut away) and the five largest $SrCrO_4$ clusters; (d) View of all clusters (rendered in different colours) with the largest cluster in blue. A, B, C indicate three different regions of the largest cluster; (e) entanglement of clusters: if tension is applied to the materials then the clusters provide a mechanical resistance improving the shear properties.

cles distributed in a polymeric matrix can form independently, but interpenetrate clusters of varying size and fractal dimension with the largest fractal dimension of 2.36 (Fig. 18).

Microstructure evolution of metal-ceramic materials Al-SiC was observed (Fig. 19) and related sintering kinetics parameters were obtained, different mechanisms of ceramic and metallic materials with microwave-dielectric loss and eddy current losses were analyzed. Further analysis of the mechanism of interfacial polarization and micro-focus were carried out. The experimental results [44] help to reveal the mixed-interaction mechanisms of microwave sintering of metal-ceramic materials and offer some significant references for actual production.

Using a special tensile testing device, high-resolution *in situ* observations showed the fracture process for randomly oriented short carbon fiber/epoxy (SCF/EP) composites. Based on this method, the response to mechanical load of two samples containing untreated SCFs or oxidation-treated SCFs were compared (Fig. 20). An increase of about 6% in the proportion of broken fibers to other types of damaged fiber in the sample with oxidation-treated fibers, was observed. Also, the oxidation treatment reduced the ineffective lengths of the composite fibers by about 20%, hence the improved mechanical properties of the composites [45].

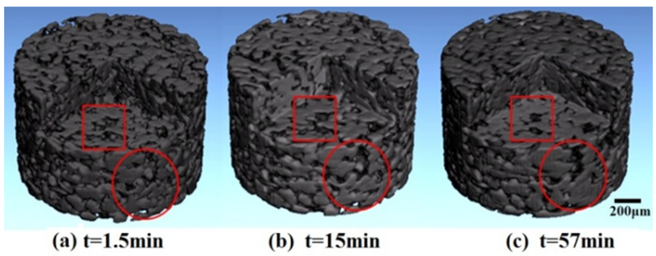

Fig. 19. (Color online) 3D structure images of SiC-Al in microwave sintering.

D. Pharmaceuticals

Structure of a pharmaceutical plays an important role in its function and effectiveness. Osmotic drug delivery systems (ODDS), delivering active agents by constant inner osmotic pressure, provide desired drug concentrations at the absorption site, maintaining the plasma drug level within the therapeutic range for a period of time, reducing the dosing frequency. The dynamic internal structural change in felodipine release process was investigated, and the remaining tablet core was correlated well with the percentages of felodipine (Fig. 21) [46, 47]. This provides the new insight to the structure-based design of ODDS. SR micro-CT was also used to monitor blend homogeneity of binary mixtures composed of microcrystalline cellulose and starch [48].

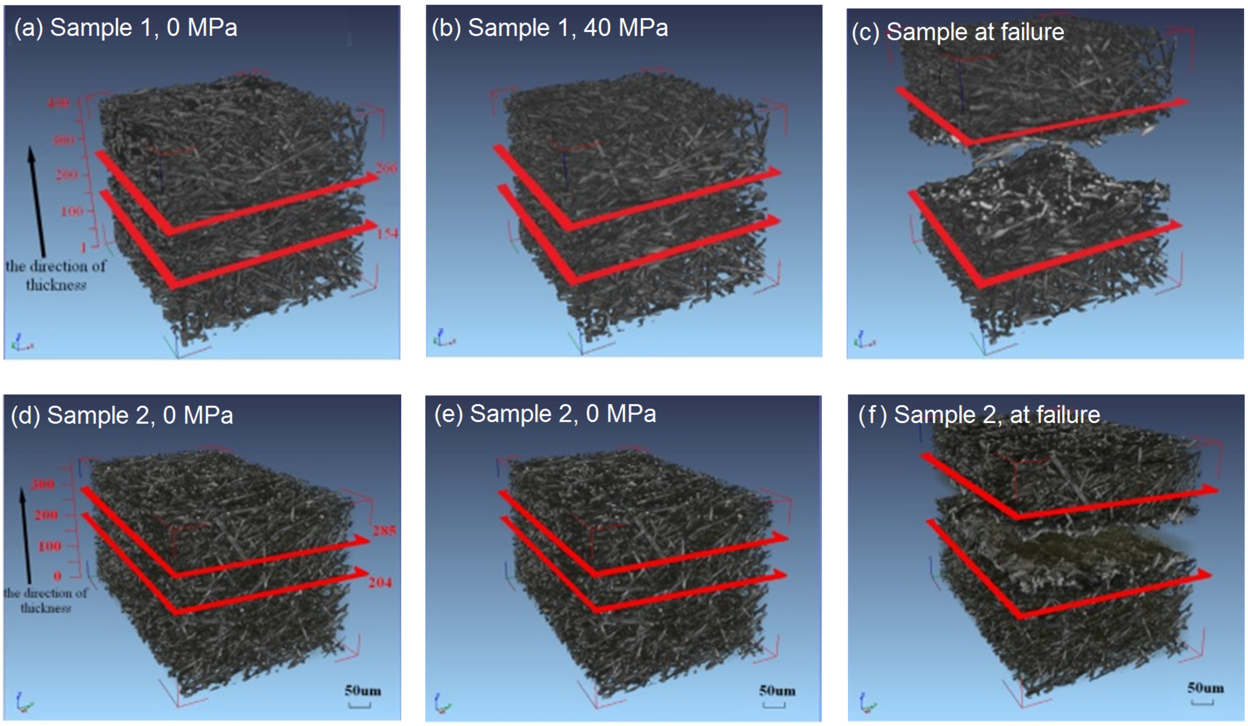

Fig. 20. (Color online) SR-CT 3D images of SCF/EP samples. Sample 1, 15% SCFs (untreated); Sample 2, 15% SCFs treated by oxidation.

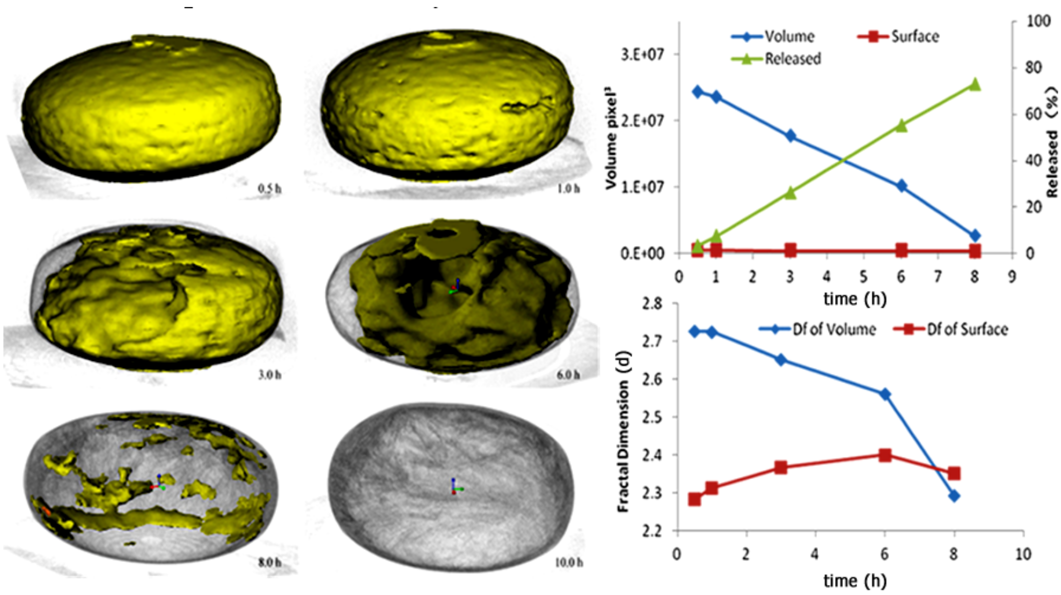

Fig. 21. (Color online) The 3D structure and quantitative analysis of controlled release kinetics of monolithic osmotic pump tablets.

E. Phytology

Identification of traditional Chinese medicines (TCMs) is an important way for quality control of TCMs. Compared with conventional microscopic identification methods, synchrotron radiation X-ray phase contrast micro-tomography (SR-XPCMT) provides clearer and finer microstructures of TCMs with better spatial and temporal resolutions nondestructively. Many investigations on different kinds of TCMs have been done since 2009 [49–51], including root and rhizome, fruit, flower, leaf, and so on. Fig. 22 shows 3D structure of a part of main root of a wild ginseng and volume distribution of the calcium oxalate cluster crystals. The distribution, quantity and volume of the calcium oxalate cluster

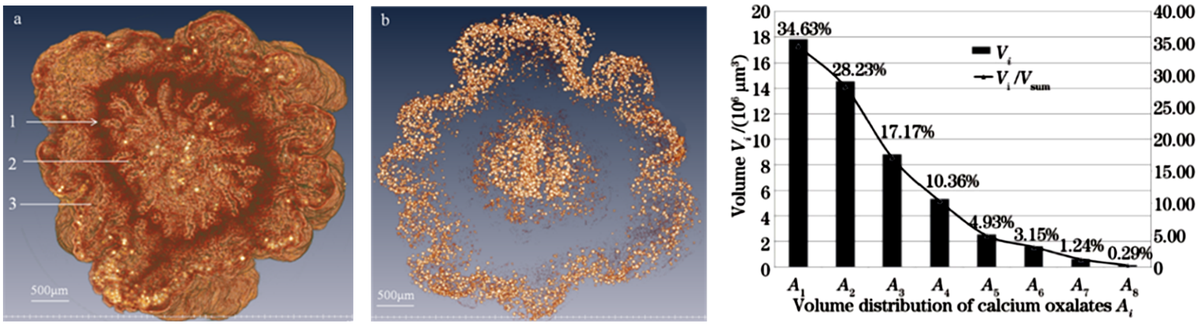

Fig. 22. (Color online) (a) 3D structure of a part of the main root of the wild ginseng; (b) 3D distribution of calcium oxalate cluster crystals; (c) Volume distribution of calcium oxalate cluster crystals of the wild ginseng main root, where V_i is the distribution volume of calcium oxalate crystals with different size of A_i and V_{sum} is the total volume of all calcium oxalate crystals.

crystals were obtained. The results show that SR-XPCMT is promising methods for identifying TCMs, especially for valuable and difficult-slicing samples. Due to its nondestructive naturer, SR-XPCMT provides the feasibility of quantitative study on microstructures of TCMs. In addition, the complex structure of bamboo nodes was revealed by the synchrotron X-ray microtomography [52] and the cavitation and water-refilling processes in plants were observed with X-ray phase contrast microscopy [53].

F. Other fields

In space science, ground calibration with high energy X-rays of BL13W1 was performed for the Gamma-Ray Burst polarimeter-POLAR, which will be the first space instrument for precise polarization measurement of Gamma-Ray Burst. Moreover, the X-ray radiation dose effects of typical optoelectronic and large-scaled processor for 20–70 keV aerospace X-rays was studied to provide reference data of ionization radiation effect for typical large-scaled processor for aerospace.

Researches in environmental science, physics, energy resources, and industrial applications were carried out on this beamline. The 3D structural characteristics and aggregation processes of farmland soil aggregates were studied, and the results revealed that different ways of fertilization in a long period could change morphology of the soil aggregate [54]. The compaction process of rods under tapping using CT method was researched to testify that the corresponding relaxation time versus tapping intensity follows an Arrhenius behaviour, which is reminiscent of the slow dynamics in thermal glassy systems [55]. The physical structure of Yangquan coal sample was characterized and the 3D visualization of compositions and volume fractions was realized. The results are relevant in quantitative modelling of coal-bed gas transportation and coal processing [56]. In the industrial applications, with 55 keV X-ray of BL13W1, 3D internal geometry of stainless steel diesel nozzle was obtained. This research has significant effect on improving the design of nozzle size and structure, and increase of the combustion efficiency [57].

VI. SUMMARY

After five years' user operation, the user community of the beamline has been built with 2/3 of them being biomedicine and material science users. And its biomedical and material science applications have gotten some remarkable achievements. Micro-CT and dynamic imaging are dominating methods. Driven by user requirements, quantitative CT imaging techniques have been developed, especially for phase retrieval in propagation based phase contrast imaging. Other X-ray methods, such as local micro-CT, a low-dose and fast micro-CT imaging method based on EST reconstruction algorithm and X-ray phase-contrast imaging with grating interferometer, are also being developed. Two new X-ray imaging beamlines, i.e. X-ray fast imaging beamline and X-ray nano-CT beamline, have been proposed in the Phase-II project of SSRF.

[1] Davis T, Gao D, Gureyev T E, *et al*. Phase-contrast imaging of weakly absorbing materials using hard X-rays. Nature, 1995, **373**: 595–598. DOI:10.1038/373595a0
[2] Wilkins S W, Gureyev T E, Gao D, *et al*. Phase-contrast imaging using polychromatic hard X-rays. Nature, 1996, **384**: 335–338. DOI:10.1038/384335a0
[3] Fitzgerald R. Phase–sensitive X–ray imaging. Phys Today, 2000, **53**: 23–26. DOI:10.1063/1.1292471
[4] Chen R C, Xie H L, Rigon L, *et al*. Phase retrieval in quantitative X–ray microtomography with a single sample-to-detector distance. Opt Lett, 2011, **36**: 1719–1721. DOI:10.1364/OL.36.001719

[5] Chen R C, Rigon L and Longo R. Comparison of single distance phase retrieval algorithms by considering different object composition and the effect of statistical and structural noise. Opt Express, 2013, **21**: 7384–7399. DOI:10.1364/OE.21.007384
[6] Ren Y Q, Chen C, Chen R C, *et al*. Optimization of image recording distances for quantitative X-ray in-line phase contrast imaging. Opt Express, 2011, 1**9** 4170–4181. DOI:10.1364/OE.19.004170
[7] Liu H Q, Ren Y Q, Guo H, *et al*. Phase retrieval for hard X–ray computed tomography of samples with hybrid compositions. Chinese Optics Letters, 2012, **10**: 121101. DOI:10.3788/COL201210.121101
[8] Wang Y D, Peng G Y, Tong Y J, *et al*. Effects of some factors on X–ray spiral micro-computed tomography at synchrotron radiation. Acta Phys Sin, 2012, **61**: 054205. (in Chinese) DOI:10.7498/aps.61.054205
[9] Deng B, Yang Q, Xie H L, *et al*. First X-ray fluorescence CT experimental results at SSRF X–ray imaging beamline. Chin Phys C, 2011, **35**: 402–404. DOI:10.1088/1674–1137/35/4/015
[10] Yang Q, Deng B, Lv W W, *et al*. Fast and accurate X-ray fluorescence CT imaging by ordered-subsets expectation maximization algorithm. J Synchrotron Radiat, 2012, **19**: 210–215. DOI:10.1107/S0909049511052253
[11] Deng B, Yang Q, Du G H, *et al*. The progress of X-ray fluorescence computed tomography at SSRF. Nucl Instrum Meth B, 2013, **305**: 5–8. DOI:10.1016/j.nimb.2013.04.045
[12] Chen W H, Wang Y D, Liu H Q, *et al*. Pseudo-global tomography for local micro-computed tomography with high–brightness synchrotron X-rays. Chin Opt Lett, 2014, **12**: 023401–023405. DOI:10.3788/col201412.023401
[13] Willner M, Herzen J, Grandl S, *et al*. Quantitative breast tissue characterization using grating-based X-ray phase-contrast imaging. Phys Med Biol, 2014, **59**: 1557–1571. DOI:10.1088/0031–9155/59/7/1557
[14] Qi J C, Ye L L, Chen R C, *et al*. Measurement of X-ray coherence of third generation synchrotron radiation. Acta Phys Sin, 2014, **63**: 104202. (in Chinese) DOI:10.7498/aps.63.104202
[15] Qi J C, Ren Y Q, Du G H, *et al*. Multiple contrast micro–computed tomography system based on X-ray grating imaging. Acta Optica Sinica, 2013, **33**: 1034001. (in Chinese) DOI:10.3788/aos20133.1034001
[16] Wang Y D, Yang Y S, Cole I, *et al*. Investigation of the microstructure of an aqueously corroded zinc wire by data-constrained modelling with multi-energy X–ray CT. Mater Corros, 2013, **64**: 180–184. DOI:10.1002/maco.201106341
[17] Wang Y D, Yang Y S, Xiao T Q, *et al*. Synchrotron-based data-constrained modeling analysis of microscopic mineral distributions in limestone. Inter J Geoscience, 2013, **4**: 344–351. DOI:10.4236/ijg.2013.42032
[18] Zhang G Q, Zhou H, He Y, *et al*. Ring artifacts correction of computerized tomography image based on polar-coordinate transform. Acta Optica Sinica, 2012, **32**: 0534001–1(6). (in Chinese) DOI:10.3788/aos201232.0534001
[19] Liu X X, Zhao J, Sun J Q, *et al*. Lung cancer and angiogenesis imaging using synchrotron. Phys Med Biol, 2010, **55**: 2399–2409. DOI:10.1088/0031–9155/55/8/017
[20] Yuan F L, Wang Y T, Guan Y J, *et al*. Real–time imaging of mouse lenticulostriate artery following brain ischemia. Front Biosci, 2013, **E5**: 517–524. DOI:10.2741/E633
[21] Liu P, Sun J Q, Zhao J, *et al*. Microvascular Imaging Using Synchrotron Radiation. J Synchrotron Radiat, 2010, **17**: 517–521. DOI:10.1107/S0909049510018832
[22] Tang R B, Yan X, Chai W M, *et al*. Microbubble-based synchrotron radiation phase contrast imaging: basic study and angiography applications. Phys Med Biol, 2011, **56** 3503–3512. DOI:10.1088/0031–9155/56/12/004
[23] Tang R B, Chai W M, Ying W H, *et al*. Anti-VEGFR2 conjugated PLGA microspheres as x-ray phase contrast agent for assessing VEGFR2 expression. Phys Med Biol, 2012, **57** 3051–3063. DOI:10.1088/0031–9155/57/10/3051
[24] Zhang D M, Yan X H, Zhang X Y, *et al*. Synchrotron radiation phase–contrast X-ray CT imaging of acupuncture points. Anal Bioanal Chem, 2011, **401** 803–808. DOI:10.1007/s00216–011–4913–7
[25] Hu J Z, Wu T D, Zeng L, *et al*. Visualization of microvasculature by X-ray in–line phase contrast imaging in rat spinal cord. Phys Med Biol,2012, **57**: N55–N63. DOI:10.1088/0031–9155/57/5/N55
[26] Li H Y, Yin X Z, Ji J Q, *et al*. Microstructural investigation to the controlled release kinetics of monolith osmotic pump tablets via synchrotron radiation X-ray microtomography. Int J Pharm, 2012, **427**: 270–275. DOI:10.1016/j.ijpharm.2012.02.017
[27] Sheng C B, Chen H Y, Wang B, *et al*. NAD+ administration significantly attenuates synchrotron radiation X-ray-induced DNA damage and structural alterations of rodent testes. Int J Physiol Pathophysiol Pharmacol, 2012, **4**: 1–9.
[28] Guan Y J, Wang Y T, Yuan F L, *et al*. Effect of suture properties on Stability of middle cerebral artery occlusion evaluated by synchrotron radiation angiography. Stroke, 2012, **43**: 888–891. DOI:10.1161/STROKEAHA.111.636456
[29] Lu H Y, Wang Y T, He X S, *et al*. Netrin–1 hyperexpression in mouse brain promotes angiogenesis and long–term neurological recovery after transient focal ischemia. Stroke, 2012, **43**: 838–43. DOI:10.1161/STROKEAHA.111.635235
[30] Dai C L, Guo H, Lu J X, *et al*. Osteogenic evaluation of calcium/magnesium–doped mesoporous silica scaffold with incorporation of rhBMP-2 by synchrotron radiation-based mCT. Biomaterials, 2011, **32**: 8506–8517. DOI:10.1016/j.biomaterials.2011.07.090
[31] Yang F, Wang J, Hou J, *et al*. Bone regeneration using cell-mediated responsive degradable PEG–based scaffolds incorporating with rhBMP-2. Biomaterials, 2013, **34**: 1514–1528. DOI:10.1016/j.biomaterials.2012.10.058
[32] Zhang J, Zhou H J, Yang K, *et al*. RhBMP-2-loaded calcium silicate/calcium phosphate cement scaffold with hierarchically porous structure for enhanced bone tissue regeneration. Biomaterials, 2013, **34**: 9381–9392. DOI:10.1016/j.biomaterials.2013.08.059
[33] Cao L Y, Wang J, Hou J, *et al*. Vascularization and bone regeneration in a critical sized defect using 2-N,6-O-sulfated chitosan nanoparticles incorporating BMP–2. Biomaterials, 2014, **35**: 684–698. DOI:10.1016/j.biomaterials.2013.10.005
[34] Yang Y M, Wang L H, Wei S Y, *et al*. Nondestructive analysis of dragonfly eye beads from the warring states period, excavated from a Chu Tomb at the Shenmingpu Site, Henan Province, China. Microsc Microanal, 2013, **19**: 335–343. DOI:10.1017/S1431927612014201
[35] Zhang X G and Pratt B R. The First Stalk-Eyed Phosphatocopine Crustacean from the Lower Cambrian of China. Curr Biol, 2012, **22**: 2149–2154. DOI:10.1016/j.cub.2012.09.027
[36] Dong Q, Zhang J, Dong J F, *et al*. *In situ* observation of columnar–to–equiaxed transition in directional solidification using synchrotron X-radiation imaging tech-

nique. Mater Sci Engineer A, 2011, **530**: 271–276. DOI:10.1016/j.msea.2011.09.085

[37] Dong Q, Zhang J, Dong J F, *et al*. Anaxial columnar dendrites in directional solidification of an Al–15 wt.% Cu alloy. Mater Lett, 2011, **65**: 3295–3297. DOI:10.1016/j.matlet.2011.07.013

[38] Xu Y, Ge X M, Tong Y J, *et al*. Kinetic Surface Roughening of Electrodeposited Amorphous PdP and NiP Films-A Comparative Study. Electrochem Commun, 2010, **12**: 442–445. DOI:10.1016/j.elecom.2010.01.015

[39] Ma H T, Qu L, Huang M L, *et al*. In-situ study on growth behavior of Ag_3Sn in Sn-3.5Ag/Cu soldering reaction by synchrotron radiation real–time imaging technology. J Alloy Compd, 2012, **537**: 286–290. DOI:10.1016/j.jallcom.2012.05.055

[40] Qu L, Zhao N, Zhao H J, *et al*. In situ study on real-time growth behavior of Cu_6Sn_5 at Sn/Cu interface during soldering reaction. Scripta Mater, 2014, **72–73**: 43–46. DOI:10.1016/j.scriptamat.2013.10.013

[41] Wang M Y, Xu Y J, Jing T, *et al*. Growth orientations and morphologies of a–Mg dendrites in Mg-Zn alloys. Scripta Mater, 2012, **67**: 629–632. DOI:10.1016/j.scriptamat.2012.07.031

[42] Xing Z, Wang M H, Du G H, *et al*. Preparation of microcellular polystyrene/polyethylene alloy foams bysupercritical CO2 foaming and analysis by X-ray microtomography. J Supercrit Fluid, 2013, **82**: 50–55. DOI:10.1016/j.supflu.2013.06.003

[43] Hughes A E, Trinchi A, Chen F F, *et al*. Revelation of intertwining organic and inorganic fractal structures in polymer coatings. Adv Mater, 2014, **26**: 4504–4508. DOI:10.1002/adma.201400561

[44] Li Y C, Xu F, Hu X F, *et al*. In situ investigation on the mixed-interaction mechanisms in the metal–ceramic system's microwave sintering. Acta Mater, 2014, **66**: 293–301. DOI:10.1016/j.actamat.2013.11.017

[45] Hu X F, Wang L B, Xu F, *et al*. In situ observations of fractures in short carbon fiber/epoxy composites. Carbon, 2014, **67**: 368–376. DOI:10.1016/j.carbon.2013.10.007

[46] Yin X Z, Li H Y, Liu R H, *et al*. Fractal structure determines controlled release kinetics of monolithic osmotic pump tablets. J Pharm Pharmacol, 2013, **65**: 953–959. DOI:10.1111/jphp.12056

[47] Yin X Z, Li H Y, Guo Z, *et al*. Quantification of swelling and erosion in the controlled release of a poorly water-soluble drug using synchrotron X-ray computed microtomography. The AAPS Journal, 2013, **15**:1025–1034. DOI:10.1208/s12248-013-9498-y

[48] Liu R H, Yin X Z, Li H Y, *et al*. Visualization and quantitative profiling of mixing and segregation of granules using synchrotron radiation X-ray microtomography and three dimensional reconstruction. Int J Pharmaceut, 2013, **445**: 125–133. DOI:10.1016/j.ijpharm.2013.02.010

[49] Xue Y L, Xiao T Q, Wu L H, *et al*. Investigation of characteristic microstructures of wild ginseng by X–ray phase contrast microscopy. Acta Physica Sinica, 2010, **59**: 5496–5507. (in Chinese)

[50] Ye L L, Xue Y L, Ni L H, *et al*. Application of X-ray phase contrast micro–tomography to the identification of traditional. Chin medicine J Instrum, 2013, **8**: C07006. DOI:10.1088/1748–0221/8/07/C07006

[51] Ye L L, Xue Y L, Tan H, *et al*. X-Ray Phase Contrast Micro–Tomography and Its Application in Quantitative 3D Imaging Study of Wild Ginseng Characteristic Microstructures. Acta Optica Sinica, 2013, **33**: 1234002(1–6). (in Chinese) DOI:10.3788/AOS201333.1234002

[52] Peng G Y, Jiang Z H, Xie H L, *et al*. Detection of complex vascular system in bamboo node by X-ray μ CT imaging technique. Holzforschung. 2014, **68**: 223–227. DOI:10.1515/hf–2013–0080

[53] Xue Y L, Xiao T Q, Du G H, *et al*. Observation of cavitation and water–refilling processes in plants with X-ray phase contrast microscopy. Nucl Sci Tech, 2013, **24**: 060101(1–6).

[54] Zhou H, Peng X H, Perfect E, *et al*. Effects of organic and inorganic fertilization on soil aggregation in an Ultisol as characterized by synchrotron based X-ray microcomputed tomography. Geoderma, 2013, **195–196**: 23–30. DOI:10.1016/j.geoderma.2012.11.003

[55] Fu Y, Xi Y, Cao Y X, *et al*. X-ray microtomography study of compaction process of rods under tapping. Phys Rev E, 2012, **85**: 051311(1–8). DOI:10.1103/PhysRevE.85.051311

[56] Wang H P, Yang Y S, Wang Y D, *et al*. Data-constrained modelling of an anthracite coal physical structure with multispectrum synchrotron X-ray CT. Fuel, 2013, **106**: 219–225. DOI:10.1016/j.fuel.2012.11.079

[57] Li Z L, Wu Z J, Gao Y, *et al*. Measurement method for diesel nozzle internal geometry and size using high-energy synchrotron radiation X-ray. J Jilin University (Engineer Tech Edition), 2011, **41**:128–132. (in Chinese)